ACS APPLIED ELECTRONIC MATERIALS

pubs.acs.org/acsaelm Article

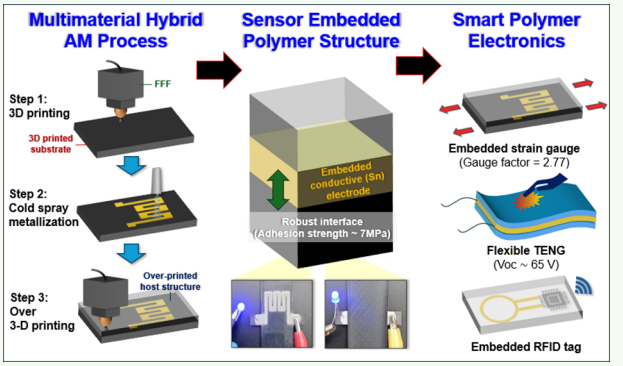
Multimaterial Hybrid Additive Manufacturing of Smart Polymer Structures with Embedded Electronics

Jaehun Jeon, SK Shamim Hasan Abir, Shinan Huang, Joni Dhar, Grace Richard, Akshay R. Ananda, Fotis Kopsaftopoulos, Johnson Samuel, and Semih Akin*

Cite This: https://doi.org/10.1021/acsaelm.6c01769 Read Online

ACCESS | Metrics & More | Article Recommendations | Supporting Information

ABSTRACT: Additive manufacturing (AM) provides a promising route for integrating electronic functionalities into polymer structures. However, existing approaches often rely on strong chemicals, post-processing, or assembly steps that limit design flexibility, manufacturing efficiency, and electrical reliability. This study presents a multimaterial hybrid AM strategy that integrates fused filament fabrication with cold spray additive manufacturing (CSAM) to fabricate polymer structures with embedded functionality. Tin (Sn) electrodes were directly deposited onto 3D-printed polymer substrates via CSAM and subsequently encapsulated through polymer over-printing, eliminating the need for surface pretreatment, thermal sintering, chemical metallization, or adhesive bonding. A systematic design of experiments with microstructural characterization established the process−structure−property relationships governing polymer metallization, identifying the optimal processing conditions for producing continuous conductive pathways with an electrical conductivity of 3.76×10^5 S·m^{-1}. The versatility of the proposed approach was demonstrated through three representative fully embedded smart structures: (i) a strain sensor with a gauge factor of 2.766; (ii) a triboelectric nanogenerator (TENG) capable of generating a peak output voltage of ∼65 V and a peak power density of 3 μW cm^{-2}; and (iii) a radio-frequency identification (RFID) circuit. These results provide a pathway toward smart polymer electronics (plastronics) for next-generation engineering systems.



KEYWORDS: *additive manufacturing, multimaterial printing, polymer electronics, smart structures, embedded sensors, material extrusion, cold spray*

1. INTRODUCTION

Polymer additive manufacturing (AM) has transformed the fabrication of customized components with enhanced geometric freedom, rapid prototyping capability, and cost-effective production.[1] More recently, advances in the internet of things (IoT), artificial intelligence (AI), and cyber-physical systems have driven a shift from passive polymer structures toward intelligent components capable of sensing, communication, and real-time data acquisition.[2−4] Hence, there is growing interest in integrating functional electronics directly into 3D-printed polymer structures for applications including structural health monitoring, wearable electronics, soft robotics, and smart manufacturing..[5−10] Realizing these applications, however, requires manufacturing strategies that can seamlessly integrate electrical functionality into 3D-printed polymer structures while preserving geometric fidelity, mechanical integrity, and manufacturing efficiency.

To achieve electrical functionality, various polymer metallization techniques have been investigated, including wet chemical plating,[11] sputter deposition,[12,13] conductive ink printing,[14,15] conductive filament-based AM,[11,16,17] and nanowire-based metallization.[18] While these approaches have successfully produced electrically conductive polymer components, they often involve strong chemicals, multiple processing steps, limited material compatibility, or poor scalability. More importantly, most studies have focused on solely surface metallization rather than the fabrication of embedded electronic architectures within polymer components. Incorporating conductive features into host components offers several advantages, including enhanced protection of electronic elements from mechanical damage, improved design flexibility, and the fabrication of compact multifunctional devices.[19] However, comparatively little attention

Received: August 14, 2026
Revised: October 21, 2026
Accepted: October 22, 2026

ACS Publications © XXXX The Author(s). Published by American Chemical Society

Downloaded from pubs.acs.org/aaemp/article-pdf/doi/10.1021/acsaelm.6c01769/6916596/7/el-2026-017696.pdf by RENSSELAER POLYTECHNIC INST user on 12 November 2026

has been devoted to embedding functional electronics directly within 3D-printed polymer structures. Achieving this capability requires robust metal−polymer bonding, reliable electrical continuity, compatibility with polymer over-printing, preservation of structural integrity, and protection of embedded electronic features. Addressing these challenges is essential for advancing the next generation of smart polymer structures with integrated sensing, communication, and energy-harvesting functionalities.

To address this gap, this study presents a hybrid AM strategy, illustrated in Figure 1, that integrates material-extrusion-based polymer 3D printing, cold spray additive manufacturing (CSAM), and polymer over-printing to fabricate multifunctional polymer structures with embedded electronics. Unlike conventional metallization techniques, CSAM deposits metallic particles through high-velocity solid-state impact rather than melting, thereby minimizing the thermal degradation of temperature-sensitive polymer substrates while promoting robust metal−polymer bonding.[20−24] Compared with conductive ink printing, aerosol jet printing, and electroless plating, which often require conductive inks, hazardous chemicals, thermal sintering, or multiple post-processing steps,[15,25−27] CSAM directly deposits metallic feedstock in a single solid-state process. In contrast to conductive filament-based approaches, which are generally limited by the low electrical conductivity of polymer composites,[16,28] CSAM produces metallic conductive pathways with higher electrical conductivity while remaining compatible with complex three-dimensional geometries.[29] Furthermore, its high deposition rate, solvent-free operation, and scalability make CSAM particularly attractive for manufacturing embedded polymer electronics. As such, the proposed strategy directly deposits conductive metallic features onto 3D-printed polymer substrates and subsequently encapsulates them through polymer over-printing without surface pretreatment, chemical metallization, thermal sintering, or secondary assembly. To the authors' knowledge, this is the first study to demonstrate a fully additive manufacturing workflow that integrates material extrusion 3D-printing (i.e., fused filament fabrication), CSAM, and polymer over-printing to fabricate fully embedded metallic electronics. The proposed approach is systematically investigated through process optimization, microstructural characterization, and functional validation using three representative embedded devices: a strain gauge, a radio-frequency identification (RFID) tag, and a flexible triboelectric nanogenerator (TENG).

Collectively, this study advances the state-of-the-art through the following contributions:

- Development of a multimaterial hybrid AM strategy that integrates FFF, CSAM, and polymer over-printing (FFF) to fabricate fully embedded smart polymer electronics.
- Establishment of the process−structure−property relationships governing CSAM-based polymer metallization.
- Demonstration of fully embedded conductive architectures without requiring surface pretreatment, thermal sintering, electroplating, or other post-deposition treatments.
- Experimental validation of the proposed AM platform through embedded strain sensing, triboelectric energy harvesting, and wireless RFID communication.

2. MATERIALS

For the material-extrusion-based fused filament fabrication (FFF) process, polylactic acid (PLA) and thermoplastic polyurethane (TPU) filaments (1.75 mm, *Creality*) were used to fabricate the polymer host structures, as illustrated in Step 1 of Figure 1. PLA was selected for its excellent dimensional stability, ease of printing, and mechanical rigidity,[30,31] whereas TPU was included because of its flexibility and elastomeric behavior,[32] enabling evaluation of the proposed manufacturing strategy on both rigid and compliant polymer substrates. For the subsequent CSAM process, a blended powder feedstock

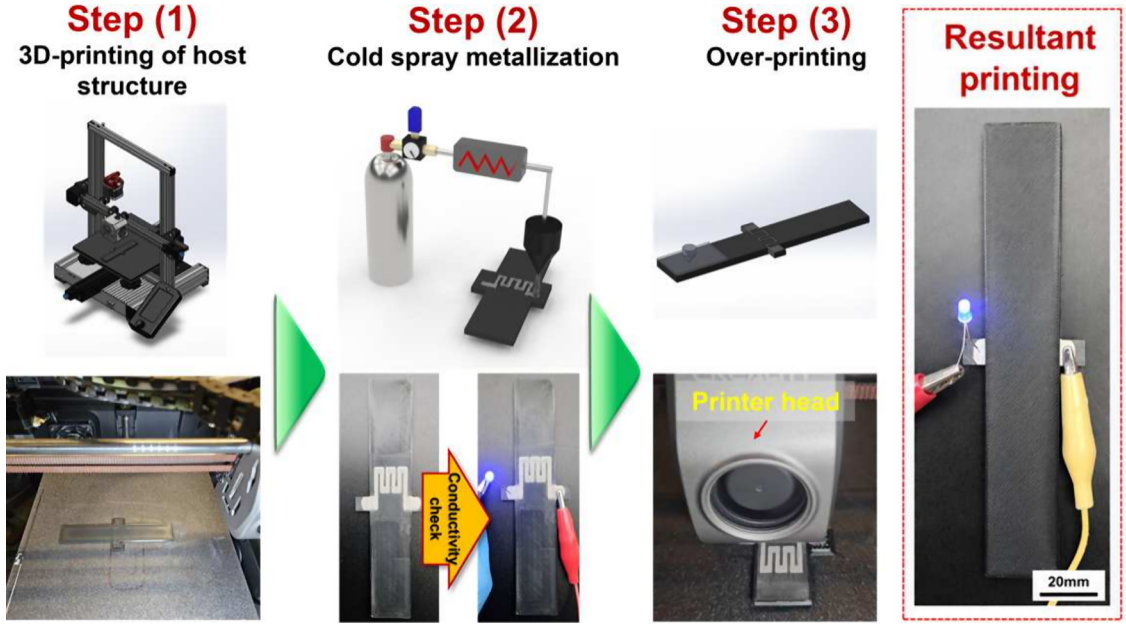


Figure 1. Proposed hybrid AM workflow for embedding conductive features and functional electronics into polymer structures through material-extrusion 3D printing, cold spray metallization, and over-printing.

Downloaded from pubs.acs.org/aaemb/article-pdf/doi/10.1021/acsaelm.6c01769/6916967/el-2026-017696.pdf by RENSSELAER POLYTECHNIC INST user on 12 November 2026

https://doi.org/10.1021/acsaelm.6c01769
ACS Appl. Electron. Mater. XXXX, XXX, XXX−XXX

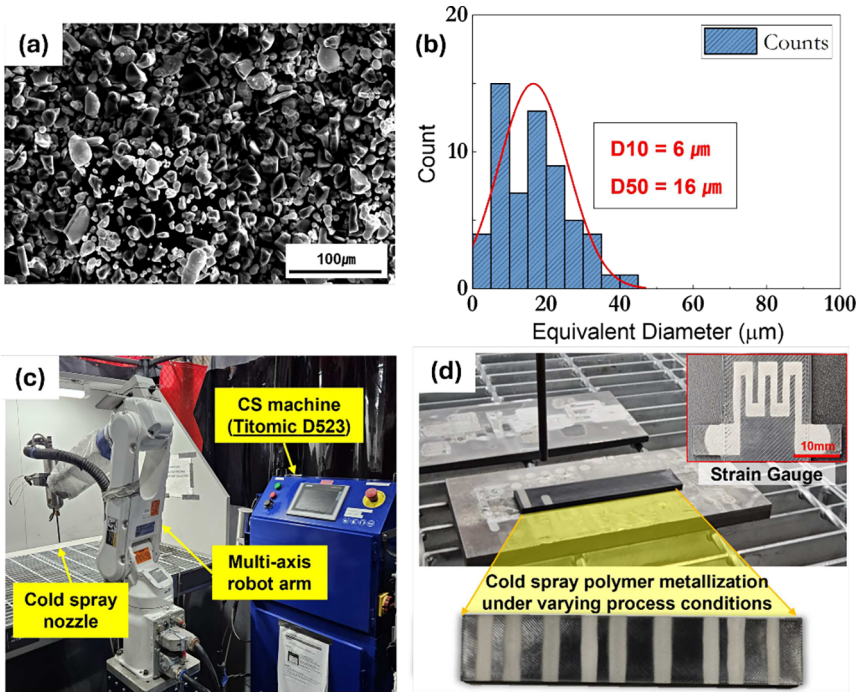


Figure 2. Cold spray polymer metallization process: (a) SEM micrograph of the Sn−Al_2O_3 feedstock powder; (b) size distribution of the feedstock powder; (c) robotic CSAM system; and (d) cold spray metallization of a polymer (PLA) substrate.

consisting of 50 wt % tin (Sn) and 50 wt % aluminum oxide (Al_2O_3) (*LPP.T-25, Titomic Inc., USA*) was used to directly deposit conductive features onto polymer substrates without the need for binders or post-processing treatments. In this feedstock, Sn serves as the ductile conductive phase, enabling the formation of electrically conductive deposits,[33] while Al_2O_3 promotes localized surface activation of the polymer substrate, thereby enhancing particle anchoring and coating adhesion during CSAM.[34] Figure 2a shows the morphology of the feedstock powders, and Figure 2b presents the corresponding particle size distribution, with a median particle diameter (d_{50}) of 16 μm. Further, EDX analysis of the feedstock powder confirmed the uniform distribution of Sn and Al_2O_3 particles, which exhibited median particle diameters of 14 and 13 μm, respectively (see Figure S1, Supporting Information).

3. METHODOLOGY

This section describes the proposed AM workflow (Figure 1), including 3D printing of the polymer host structures, CSAM for the deposition of conductive patterns, and the subsequent polymer over-printing process used to fabricate fully embedded electronics. The processing parameters for each manufacturing step are given in Table 1.

3.1. 3D-Printing of the Host Structure

The host polymer structure was 3D-printed using the FFF process (Figure 1, Step-1). A commercial desktop 3D printer (*Creality K1C*) equipped with a 0.4 mm nozzle was utilized for the fabrication process. Both PLA and TPU structures were fabricated using a 100% infill density. During printing, the bed temperature was maintained at 50 °C for PLA and 35 °C for TPU, while the extruder temperature was set to 230 °C for both PLA and TPU. For both materials, a printing speed of 250 mm s^{-1} was employed, whereas the first-layer printing speed was reduced to 60 mm s^{-1} to enhance bed adhesion and dimensional stability.

Table 1. Processing Parameters Used in the FFF and CSAM Processes

procedure	parameter	setting	unit
(1) FFF	filament diameter	1.75	mm
	bed temperature	50	°C
	extruder temperature	230	°C
	infill density	100	%
	layer height	0.2	mm
	print speed	250	mm/s
	first-layer speed	60	mm/s
(2) cold spray	driving gas	Air	–
	gas pressure	0.5, 0.6	MPa
	gas temperature	100, 150, 200	°C
	nozzle traverse speed	100, 150	mm/s
	nozzle stand-off distance	15	mm
(3) FFF over-print	same as (1)	same as (1)	same as (1)

3.2. CSAM of Electrodes (Polymer Metallization)

Following fabrication of the host structure, sensors and interconnects were deposited by CSAM. CSAM is a solid-state deposition process in which metallic or composite powder particles are accelerated to supersonic velocities using compressed and heated gas, enabling material deposition through high-velocity particle impacts.[35,36] This unique deposition mechanism makes CSAM particularly well suited for metallizing polymer substrates, enabling the direct fabrication of conductive features with minimal thermal degradation.[23,33] The deposition

Downloaded from pubs.acs.org/aaemp/article-pdf/doi/10.1021/acsaelm.6c01769/6916596/7/el-2026-017696.pdf by RENSSELAER POLYTECHNIC INST user on 12 November 2026

https://doi.org/10.1021/acsaelm.6c01769
ACS Appl. Electron. Mater. XXXX, XXX, XXX−XXX

process was carried out using a low-pressure robotic CSAM system (*Titomic D523*), as shown in Figure 2c. Compressed and heated air served as the process gas to accelerate the powder particles toward the polymer substrate, enabling the direct writing of conductive features onto the 3D-printed structures (Figure 2d). To establish the processing conditions required for high-quality metallization, a full-factorial design of Experiments (DoE) was conducted to systematically investigate the effects of key process parameters (i.e., gas pressure, gas temperature, nozzle traverse speed). The quality of the deposited features was assessed in terms of deposition resolution, coating continuity, and electrical resistance to identify the optimal processing window for fabricating conductive patterns on polymer substrates.

3.3. Over 3-D Printing

Following CSAM, an over 3-D printing process was performed to encapsulate the conductive features and realize fully embedded sensing architectures. The overprinting process was carried out using the same FFF system and processing parameters employed for fabrication of the polymer host structures (Table 1). During overprinting, additional polymer layers were deposited directly onto the CSAM-patterned surfaces, embedding the conductive features within the polymer matrix while providing mechanical protection against external damage. Careful alignment between the conductive features and the overprinted polymer layers was maintained to preserve electrical continuity and structural integrity. To facilitate external electrical interfacing and functional testing, selected electrode regions were intentionally left exposed (Figure 1, right panel). Overall, the integrated material-extrusion and CSAM workflow enabled the fabrication of fully additively manufactured polymer structures with embedded functionality. Video S1 (Supporting Information) demonstrates the overprinting of CSAM conductive features during the 3D-printing process.

3.4. Characterization

The fabricated conductive features and devices were characterized to evaluate their morphological, electrical, and functional performance. Surface morphology, coating quality, and coating thickness were examined using scanning electron microscopy (SEM, *Zeiss, SUPRA 55*), with coating thickness quantified from SEM micrographs using *ImageJ* software. Energy-dispersive X-ray spectroscopy (EDX), integrated with the SEM system, was employed to characterize the elemental composition and spatial distribution of the deposited coatings. The electrical performance of the electrodes was evaluated by measuring electrical resistance with a digital multimeter (*Agilent, 34405A*).

Functional characterization was subsequently performed to evaluate the sensing performance of the embedded devices. Electrical signals were acquired through the exposed electrode interfaces incorporated during the polymer overprinting process. For the embedded strain gauge, uniaxial tensile tests were conducted using a universal testing machine (*Instron 4204*). The electrical resistance was continuously monitored as a function of the applied strain to evaluate strain sensitivity, signal stability, and device integrity. For the embedded radio-frequency identification (RFID) device, an Arduino-based interface was developed for signal acquisition and wireless communication, enabling functional evaluation of the embedded RFID system.

The energy-harvesting performance of the embedded triboelectric nanogenerator (TENG) was evaluated using a custom-built programmable pneumatic actuator. The open-circuit voltage (V_{oc}) was measured with an oscilloscope (*Agilent, DSO1014A*), while the short-circuit current (I_{sc}) was measured using a current amplifier (*Edmund Optics*) interfaced with the oscilloscope. Cyclic mechanical loading was applied at excitation frequencies of 0.5, 1, and 2 Hz to evaluate the electrical output and dynamic response of the fabricated TENG devices.

4. RESULTS AND DISCUSSION

4.1. Design of Experiments (DoE)

A full-factorial DoE was employed to evaluate the influence of key CSAM process parameters on the quality of polymer metallization. Gas temperature, gas pressure, and nozzle traverse speed were selected as the primary process variables. As summarized in Table 2, gas temperature was investigated at three levels, whereas gas pressure and nozzle traverse speed were each evaluated at two levels. For the polymer substrate, 3D-printed PLA substrates were used throughout the study. This experimental design provided a comprehensive assessment of both the individual and interactive effects of the process parameters on deposition performance, as quantified by deposition resolution (line width) and electrical resistance. Each experimental condition was repeated three times using single-pass deposition, and both responses were measured over 20 mm coating length. The experimental results are summarized in Table 3.

Figure 3 presents the effects of gas temperature, gas pressure, and nozzle traverse speed on the deposition resolution (line width) and electrical performance of the cold-sprayed coatings. Contour plots (Figure 3a–d) were generated to visualize the combined influence of temperature and nozzle speed at two gas pressures (0.5 and 0.6 MPa). The line width was found to increase primarily with increasing gas temperature. At both gas pressures, increasing the gas temperature from 100 to 200 °C resulted in a continuous increase in the deposited line width, from ∼5.5 to 7.3 mm. This behavior is attributed to enhanced plastic deformation of the ductile (i.e., Sn-rich) particles at elevated temperatures, resulting in wider deposition tracks. In contrast, increasing the pressure from 0.5 to 0.6 MPa had little effect on line width, indicating that temperature is the primary factor governing deposition resolution. Similarly, nozzle traverse speed had a minor influence on line width, with slightly narrower tracks observed at higher nozzle speeds.

Table 2. Full-Factorial Design of Experiment (DoE) and Corresponding Responses[a]

variable	parameter	value	unit
independent variables	gas temperature (T)	100, 150, 200	°C
	gas pressure (P)	0.5, 0.6	MPa
	nozzle traverse speed (V)	100, 150	mm/s
response 1	resistance		Ω
response 2	line width		mm
replicates		3	
total experimental runs		36	

[a]Note: Fixed parameters were a nozzle stand-off distance of 15 mm and one spray pass.

Downloaded from pubs.acs.org/aaemb/article-pdf/doi/10.1021/acsaelm.6c01769/6916596/7/el-2026-017696.pdf by RENSSELAER POLYTECHNIC INST user on 12 November 2026

https://doi.org/10.1021/acsaelm.6c01769
ACS Appl. Electron. Mater. XXXX, XXX, XXX–XXX

Table 3. Respective Results of the Design of Experiment (DoE) Analysis

parameter	width [mm]	resistance [Ω]	parameter	width [mm]	resistance [Ω]
100 °C	5.2	60.6	100 °C	5.7	0.21
100 mm/s	6.0	57.2	150 mm/s	5.8	0.23
0.5 MPa	5.2	21.3	0.5 MPa	5.5	0.25
100 °C	5.9	0.65	100 °C	5.5	0.18
100 mm/s	5.9	0.38	150 mm/s	5.5	0.24
0.6 MPa	5.7	0.36	0.6 MPa	5.7	0.23
150 °C	6.0	6.8	150 °C	6.3	0.17
100 mm/s	6.1	1.7	150 mm/s	6.6	0.14
0.5 MPa	6.0	2.4	0.5 MPa	6.7	0.16
150 °C	6.9	0.2	150 °C	6.5	0.18
100 mm/s	7.0	0.18	150 mm/s	6.7	0.13
0.6 MPa	7.1	0.23	0.6 MPa	6.5	0.14
200 °C	7.6	0.23	200 °C	7.0	0.16
100 mm/s	7.8	0.65	150 mm/s	7.4	0.13
0.5 MPa	7.4	0.23	0.5 MPa	6.9	0.16
200 °C	7.4	0.23	200 °C	7.1	0.15
100 mm/s	7.4	0.19	150 mm/s	7.2	0.14
0.6 MPa	7.3	0.18	0.6 MPa	7.5	0.14

The electrical resistance exhibited a substantially stronger dependence on the processing parameters than the deposition width. As illustrated in Figure 3b,d, increasing either the gas temperature or gas pressure significantly reduced the electrical resistance of the deposited conductive traces. The highest resistance values were observed at the lowest processing condition (100 °C and 0.5 MPa), whereas the resistance progressively decreased with increasing temperature and approached its minimum value at 200 °C. This behavior can be explained by the higher particle velocities and kinetic energies generated under elevated gas temperatures and pressures, allowing a greater fraction of the Sn-rich particles to exceed the critical deposition velocity required for bonding. Upon impact, the particles undergo more extensive plastic deformation, producing larger contact areas between neighboring particles and enhancing mechanical interlocking with the polymer substrate. These effects improve coating continuity, reduce interparticle contact resistance, and establish more efficient conductive pathways throughout the deposited layer. As such, the enhanced particle consolidation translates directly into the lower electrical resistance observed under the optimized processing conditions.

To statistically assess the influence of the processing parameters on each response, an analysis of variance (ANOVA) was conducted. The analysis considered the main effects (i.e., gas pressure (P), gas temperature (T), and nozzle speed (V) and interaction terms (i.e., T^2, PV, PT, VT, VTP). Only the main effects (T, P, V) were found to be statistically significant, whereas the interaction terms were not (see Table S1, Supporting Information). Based on these results, the main-effect plots shown in Figure 3e,f were used to quantify the relative influence of each main processing parameter. For line width, gas temperature exhibited the greatest effect, followed by gas pressure, whereas nozzle traverse speed had only a minor influence. A similar trend was observed for electrical resistance, with gas temperature producing the largest reduction in resistance and increased gas pressure further improving electrical conductivity. In contrast, nozzle traverse speed had the smallest overall effect on both responses. Based on the DoE analysis, the best-performing CSAM parameters within the investigated process space were selected by minimizing electrical resistance while maximizing nozzle traverse speed to enhance both metallization performance and manufacturing throughput. Accordingly, the optimal processing condition was identified as a gas temperature of 200 °C, a gas pressure of 0.6 MPa, and a nozzle traverse speed of 150 mm/s.

In addition, the thermal and mechanical effects of the CSAM process parameters on the PLA substrate were evaluated through stationary nozzle tests conducted on 3-and 4-mm thick 3D-printed PLA substrates at three processing conditions: 200 °C-0.6 MPa, 200 °C-0.5 MPa, and 100 °C and 0.6 MPa, with a stand-off distance of 15 mm (see Video S3, Supporting Information). For both substrate thicknesses, visible surface damage initiated within 3 to 5 s under the 200 °C conditions, regardless of gas pressure, whereas only negligible damage was observed at 100 °C and 0.6 MPa. Infrared thermography (*FLIR C8*, emissivity = 0.93) revealed peak surface temperatures of ∼120 to 140 °C for the 200 °C cases and 70 to 80 °C for the 100 °C condition. These observations indicate that gas temperature has a more pronounced influence on substrate damage than gas pressure. The results further suggest that when operating at elevated gas temperatures (e.g., 200 °C), a sufficiently high nozzle traverse speed is necessary to minimize localized thermal exposure and mitigate thermally induced damage to the polymer substrate.

4.2. Microstructural and Electrical Characterization

To evaluate the influence of CSAM processing parameters on coating quality, microscopy characterizations were performed on specimens fabricated under two representative processing conditions: the optimal condition (200 °C, 0.6 MPa, 150 mm/s) and a lower-performance condition (100 °C, 0.5 MPa, 100 mm/s). These conditions corresponded to the parameter combinations exhibiting the highest and lowest electrical conductivities, respectively, as identified through the DoE analysis. Optical microscopy of the deposited coatings (Figure 4a,b) revealed a broader deposition track under the optimal condition (6.8−7.4 mm) than under the lower-performance condition (4.5−5.0 mm). The optimal condition also produced well-defined deposition boundaries and a more uniform coating, indicating improved coating uniformity and

Downloaded from pubs.acs.org/aaembp/article-pdf/doi/10.1021/acsaelm.6c01769/6916596/7/el-2026-017696.pdf by RENSSELAER POLYTECHNIC INST user on 12 November 2026

https://doi.org/10.1021/acsaelm.6c01769
ACS Appl. Electron. Mater. XXXX, XXX, XXX−XXX

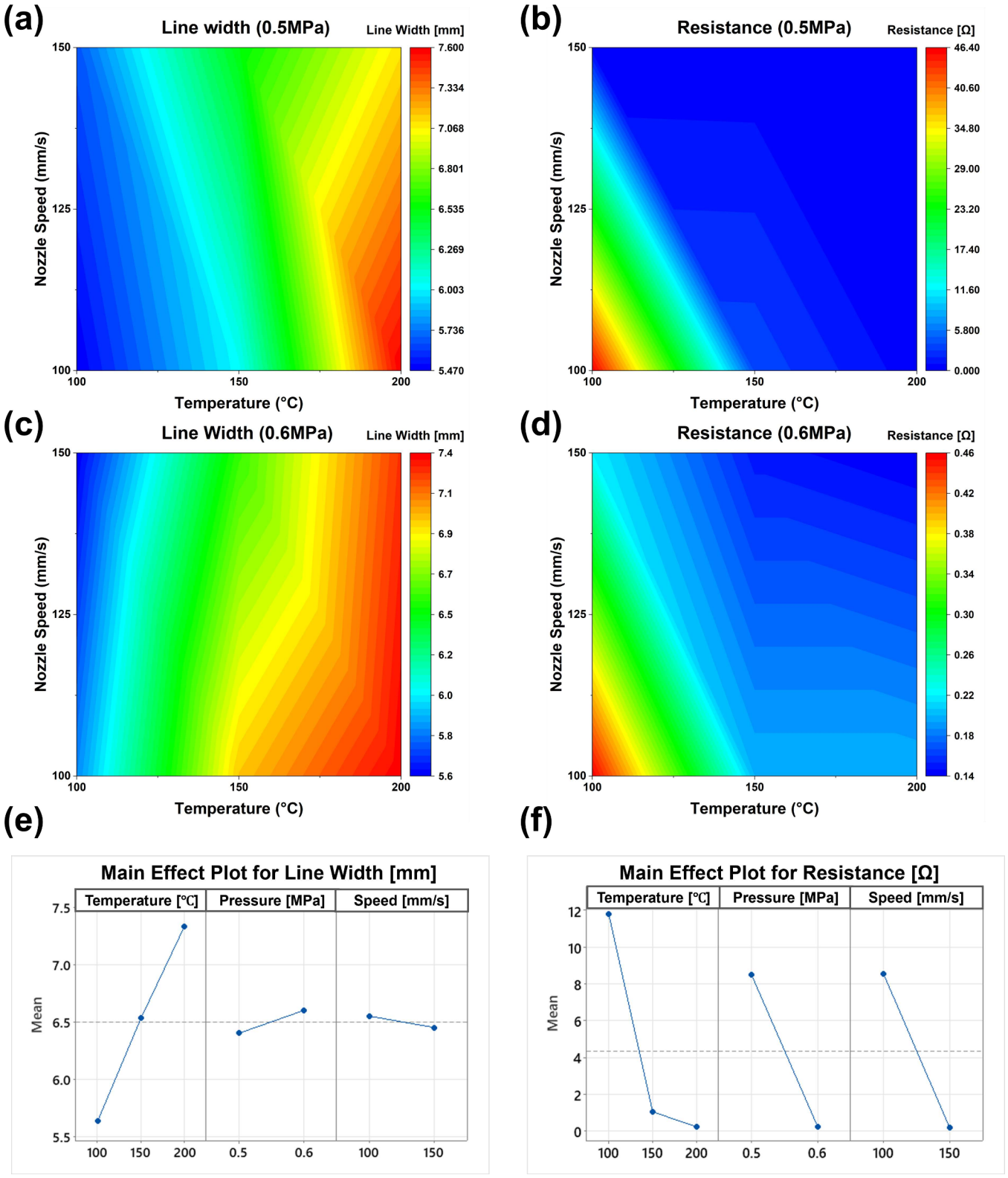


Figure 3. Parametric analysis of the cold spray metallization process. Contour plots showing the combined effects of gas temperature and nozzle traverse speed on (a) line width at 0.5 MPa, (b) electrical resistance at 0.5 MPa, (c) line width at 0.6 MPa, and (d) electrical resistance at 0.6 MPa. Main-effect plots illustrating the influence of gas temperature, gas pressure, and nozzle traverse speed on (e) line width and (f) electrical resistance.

Downloaded from pubs.acs.org/aaembp/article-pdf/doi/10.1021/acsaelm.6c01769/6916596/el-2026-017696.pdf by RENSSELAER POLYTECHNIC INST user on 12 November 2026

https://doi.org/10.1021/acsaelm.6c01769
ACS Appl. Electron. Mater. XXXX, XXX, XXX–XXX

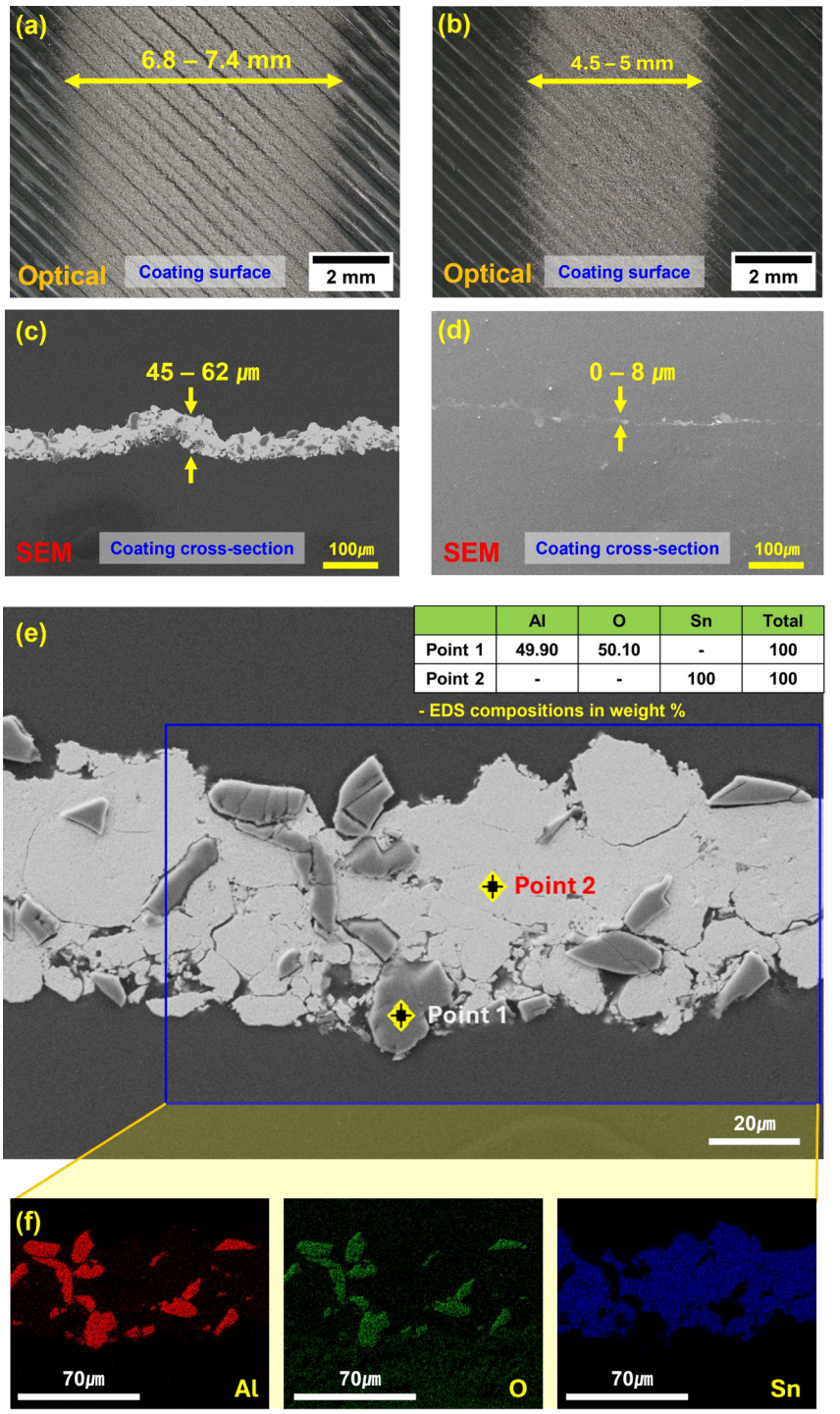


Figure 4. Microstructural characterization of CSAM polymer metallization. Surface morphology obtained under (a) optimal processing conditions and (b) lower-performance conditions; cross-sectional SEM images of coatings deposited under (c) optimal and (d) lower-performance conditions; (e) higher-magnification cross-sectional microstructure of the optimized coating; and (f) corresponding EDS maps of the coating.

surface coverage. These improvements are attributed to the higher particle velocities generated by the elevated gas temperature and pressure, which enhance particle dispersion and promote coating continuity on the polymer substrate.

The corresponding cross-sectional SEM images (Figure 4c,d) further demonstrated the influence of the processing conditions on coating formation. Under the optimal condition, a continuous and well-consolidated coating with a thickness ranging from 45 to 62 μm was produced (Figure 4c). The intimate contact observed at the coating−substrate interface is consistent with effective mechanical interlocking between the deposited particles and the polymer substrate (PLA). Moreover, no discernible interfacial gaps or delamination were observed in the optimized coating, suggesting robust and strong interfacial integrity. This effective interfacial bonding is particularly important for embedded electronics, as it helps maintain electrical continuity during

https://doi.org/10.1021/acsaelm.6c01769
ACS Appl. Electron. Mater. XXXX, XXX, XXX−XXX

Downloaded from pubs.acs.org/aaembp/article-pdf/doi/10.1021/acsaelm.6c01769/6916967/el-2026-017696.pdf by RENSSELAER POLYTECHNIC INST user on 12 November 2026

the subsequent polymer over-printing process and under mechanical loading. In contrast, the lower-performance condition produced a thin, discontinuous coating with a thickness ranging from 0 to 8 μm (Figure 4d), and several regions exhibited no measurable deposition. These observations indicate that the lower gas temperature and pressure were insufficient to achieve reliable coating formation, resulting in discontinuous conductive pathways and a substantially higher measured electrical resistance (46.4 Ω).

To further verify the composition of the deposited coating, EDX point analysis and elemental mapping were performed on the specimen fabricated under optimal processing conditions. As shown in Figure 4e,f, the EDX point analysis confirmed the expected constituents of the Sn/Al_2O_3 blended feedstock. Point 1 exhibited Al (49.90 wt %) and O (50.10 wt %), corresponding to the Al_2O_3 phase, whereas Point 2 consisted entirely of Sn (100 wt %), representing the conductive metallic phase. The elemental maps revealed the distribution of the Sn and Al_2O_3 phases throughout the coating. The distributed Sn-rich regions provided conductive pathways for electron transport, while the phase distribution is consistent with the well-consolidated coating observed in the SEM images.

Overall, the microstructural observations establish a clear process−structure−property relationship for CSAM-based polymer metallization. Higher gas temperature and pressure enhance particle deformation and deposition efficiency, producing thicker, more continuous coatings with improved particle connectivity, thereby reducing electrical resistance and increasing conductivity. In contrast, insufficient particle impact energy results in discontinuous coatings with poor particle bonding and degraded electrical performance. These findings demonstrate that controlling particle impact conditions is critical for optimizing the electrical performance of CSAM polymer electronics.

The electrical conductivity was calculated using eq 1, where σ is the electrical conductivity (S m^{-1}), L is the coating length (m), R is the measured electrical resistance (Ω), and A is the coating cross-sectional area (m^2), determined from the measured coating width and thickness.

$$\sigma = \frac{L}{RA} \tag{1}$$

Using an average coating thickness of 53.5 μm, a width of 7.1 mm, a length of 20 mm, and an electrical resistance of 0.14 Ω, the electrical conductivity of the coating fabricated under the optimized processing conditions was estimated to be 3.76×10^5 S·m^{-1}. Although this value is lower than that of bulk tin (Sn) (~9.17×10^6 S·m^{-1}),[24] it remains within one order of magnitude of bulk Sn. It should also be noted that the intrinsic conductivity of Sn is lower than that of bulk Cu and Ag, which might limit its suitability for applications requiring low-loss power transmission or high-current conduction. Nevertheless, many printed electronic devices (e.g., resistive strain gauges, structural-health-monitoring sensors, conductive signal pathways) operate at relatively low currents, making the demonstrated approach suitable for integrating functional features into 3D-printed polymer structures, as discussed in Section 4.4.

Table 4 compares the electrical conductivity achieved in the present study with those reported for state-of-the-art additively manufactured polymer electronics (plastronics). Despite the absence of any post-deposition treatment, the proposed approach achieved higher electrical conductivity than many previously reported studies (Table 4). Notably, most existing studies employed copper (Cu) or silver (Ag)-based metallization systems, often coupled with additional processing steps (e.g., etching, chemical plating, post-deposition annealing) to achieve high electrical conductivity.[11,17,37] In contrast, the proposed CSAM process directly deposits conductive features onto 3D-printed polymer substrates in a single solid-state manufacturing step using low-cost Sn feedstock rather than Cu or Ag. As such, this solvent-free approach eliminates the need for multiple post-processing steps while offering a scalable and cost-effective route for fabricating polymer electronics.

4.3. Patterning Fidelity and Coating Integrity

To evaluate patterning fidelity, which is an important factor governing device performance, a serpentine-shaped (i.e., strain gauge) electrode was considered as a representative test specimen. Six regions along the electrode strands were characterized using a 3D profiling microscope (*Zeta, zeta-20*) at 5× magnification. Cross-sectional profile roughness (R_a) and strand width were measured at multiple locations within each region to assess surface uniformity and dimensional accuracy (see Figures 5a and S3, Supporting Information). The average surface roughness was 20.99 μm with a standard deviation of 4.40 μm (see Figure 5a, top-right panel). In addition, the average strand width was 1602.2 μm, which was slightly larger than

Table 4. Benchmark Comparison of State-of-the-Art Additively Manufactured Polymer Electronics (Plastronics)[a]

AM process	metallization method	substrate	electrode material	material preparation	electrode thickness [μm]	electrical conductivity [S m^{-1}]	reference
FFF	CSAM	PLA	Sn	none (direct writing)	45−62	3.76×10^5	this study
FFF	electroless plating	ABS	Cu	conductive filament	5−15	1.67×10^4	11
FFF	electroless plating	ABS	Cu	dip coating	57.93	3.30×10^5	17
FFF	RF sputtering	PLA	Al	surface treatment	1	3.2×10^5	13
VAT	Filler embedding	resin	AgNW	freeze dry and dispersion	600 (bulk)	11	18
VAT	electroless plating	PLCD-F + libethenite	Cu	laser activation	NA	2.04×10^7	37
VAT	electroless plating	resin	Ni and Cu	precursor mixing	2.07 (Ni)	3.01×10^5 (Ni), 1.69×10^7 (Cu)	38
VAT	electroless plating	resin	Cu	sand blasting and sanding	5−50	4.44×10^7 (Cu)	39

[a]Note: For each study, the highest reported electrical conductivity is listed. VAT denotes vat polymerization.

https://doi.org/10.1021/acsaelm.6c01769
ACS Appl. Electron. Mater. XXXX, XXX, XXX−XXX

Downloaded from pubs.acs.org/aaemp/article-pdf/doi/10.1021/acsaelm.6c01769/6916596/7/el-2026-017696.pdf by RENSSELAER POLYTECHNIC INST user on 12 November 2026

the target value of 1500 μm (see Figure 5a, bottom-right panel). This deviation may be attributed to particle smearing and lateral spreading beneath the mask edges during the cold spray process.[40] Nevertheless, the relatively small standard deviation in strand width (44.3 μm) indicates consistent pattern formation across the evaluated regions.

The integrity of the CSAM layer was further evaluated using ASTM D3359 (Method B) cross-cut and ASTM D4541 pull-off adhesion tests, with representative images provided in Figure S4 (Supporting Information). As shown in Figure 5b, three replicate cross-cut tests exhibited negligible coating removal along the cut edges and intersections, corresponding to strong adhesion strength with a 5B classification. The coating adhesion strength was subsequently quantified through pull-off testing (Figure 5c). The three tests yielded pull-off strengths of 7.23, 7.11, and 6.66 MPa, corresponding to an average of 7.00 ± 0.30 MPa. This value is comparable to previously reported pull-off strengths for cold spray metallization of polymeric substrates, including approximately 5.6 MPa for PC/Sn, 6 MPa for PA6/Sn, and 7.6 MPa for CFRP/Sn interfaces.[20] The post-test surfaces of the PLA substrate and dollies exhibited similar failure behavior across the three tests (see Figure 5c).

In addition, the interlayer adhesion between the overprinted PLA and CSAM coating was evaluated. To minimize mechanical support from the surrounding monolithic PLA and localize the tensile load at the overprinted interface, a 20 mm × 22 mm region surrounding the test area was partially cut to approximately half the beam thickness (see Figure S5, Supporting Information). Three replicate tests yielded an average adhesion strength of 3.08 ± 0.12 MPa. This value is comparable in magnitude to previously reported adhesion strengths for FFF-fabricated PLA interfaces. Parodo et al.[41] reported an average pull-off strength of ∼5.6 MPa for untreated FFF-printed PLA using a confined 20 mm × 20 mm test region. Similarly, PLA−metal interfaces fabricated by directly printing PLA onto metallic substrates have been reported to exhibit perpendicular tensile adhesion strengths of approximately 1−2 MPa.[42] Taken together, these results demonstrate measurable and repeatable adhesion at both critical interfaces: (i) between the CSAM layer and the underlying PLA substrate and (ii) between the coating and the overprinted PLA. These findings support the structural integrity of the proposed metallization−overprinting approach for fabricating integrated conductive features within 3D-printed polymer components.

4.4. Functional Validation of the Hybrid AM Platform

To demonstrate the versatility of the proposed AM approach, three representative smart polymer structures were designed, fabricated, and evaluated. These include: (i) an embedded strain gauge for mechanical sensing, (ii) an embedded TENG for energy harvesting, and (iii) an RFID circuit for wireless communication.

4.4.1. Embedded Strain Sensing. To demonstrate the feasibility of the proposed AM approach for embedded sensing, a strain gauge (SG) was designed as an application. The SG featured five end loops and a strand width of 1.5 mm, based on a previous systematic study of the effects of end-loop number, strand width, and printing orientation on sensing performance[16] (see Figure S2a, Supporting Information). The SG pattern, with exposed connection electrodes, was fabricated on a 3D-printed PLA substrate via CSAM using a metal mask (Figure S2b, Supporting Information). The deposited SG was subsequently embedded within the polymer host structure by over-printing, leaving only the connection electrodes exposed for electrical measurements (Figure 6a). Overall, three embedded SGs were fabricated to validate the feasibility and reproducibility of the overprinting workflow. The fabricated SGs exhibited similar resistance values of 0.64, 0.73, and 0.81 Ω, indicating comparable reproducibility among the devices. One of the embedded SG devices was subsequently selected for further electrical performance evaluation. The sensing performance of the embedded SG was evaluated under stepwise quasi-static tensile loading using a universal testing machine (*Instron 4204*), while its electrical resistance was continuously monitored using a four-wire resistance measurement system (*Agilent, 34401A*). During testing, the tensile load was increased from 0 to 800 N in 100 N increments, with each load level maintained for 2 min. A commercial foil SG (*Omega, KFH-6-350-C1-11L1MR2*) was bonded to the specimen surface (Figure 6b) and measurement data were acquired through a DAQ system (*National Instruments-9236*) to provide the reference strain required for calibration and performance validation.

Figure 6c presents the strain response from the commercial foil SG and Figure 6d shows normalized resistance variation of the embedded SG during the quasi-static tensile test. For visualization purposes, the raw resistance data were smoothed using a 100-point moving-average filter.[43] The embedded sensor exhibited stable and repeatable stepwise resistance increases corresponding to each applied load increment, indicating that the CSAM-conductive network remained electrically continuous throughout mechanical deformation. No abrupt signal fluctuations or electrical discontinuities were observed, confirming that the metallized layer preserved its electrical integrity after the over-printing process.

The gauge factor (GF) of the embedded SG was determined to be 2.766 using the reference strain measured by the commercial SG according to eq 2, where R_0 is the initial electrical resistance, ΔR is the resistance change, and ε is the applied mechanical strain. The measured GF is comparable to that of commercial metallic foil SGs, which typically exhibit GF of ∼2.0−2.2.[44] The measured resistance changes were then converted into strain values using the calculated GF and compared with the reference strain obtained from the commercial SG (Figure 6d,e). The predicted strain showed good agreement with the reference measurements throughout the loading sequence, demonstrating the ability of the embedded SG to monitor mechanical deformation while remaining fully integrated within the polymer structure. The minor discrepancies observed between the embedded and commercial SGs (Figure 6e) can be attributed to differences in their sensing architectures. In detail, commercial SGs employ continuous metallic foils with highly uniform geometries, whereas the CSAM-fabricated sensor consists of a particulate metallic network deposited onto an uneven 3D-printed substrate and further embedded within a polymer matrix (see Figure 6a,b). As such, under mechanical loading, changes in electrical resistance arise not only from geometric deformation but also from variations in interparticle contact resistance and the inherent anisotropy of the CSAM-fabricated sensing layer (see Figure S6a,b, Supporting Information). These factors introduce slight nonlinearities and directional variations in the electromechanical response compared with conventional foil strain gauges. Nevertheless, the embedded sensor accurately tracked the

Downloaded from pubs.acs.org/aaemb/article-pdf/doi/10.1021/acsaelm.6c01769/6916596/7/el-2026-017696.pdf by RENSSELAER POLYTECHNIC INST user on 12 November 2026

https://doi.org/10.1021/acsaelm.6c01769
ACS Appl. Electron. Mater. XXXX, XXX, XXX−XXX

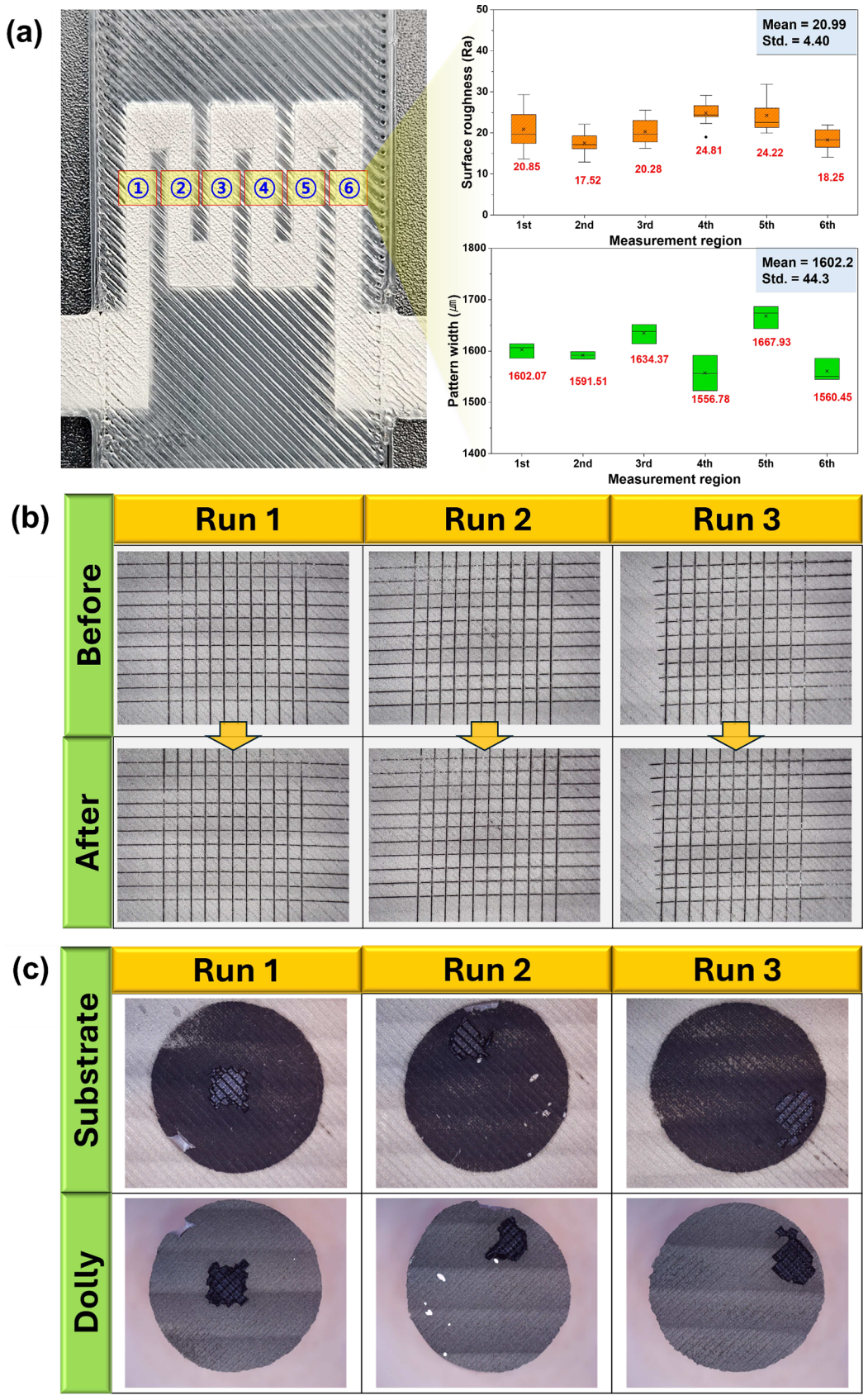


Figure 5. Pattern fidelity and coating integrity evaluation: (a) image of the pattern fidelity test specimen (left panel), surface roughness measurements (top-right panel), and pattern width measurements (bottom-right panel); (b) cross-cut adhesion test results; and (c) pull-off adhesion test results.

Downloaded from pubs.acs.org/aaembp/article-pdf/doi/10.1021/acsaelm.6c01769/6916967/el-2026-017696.pdf by RENSSELAER POLYTECHNIC INST user on 12 November 2026

https://doi.org/10.1021/acsaelm.6c01769
ACS Appl. Electron. Mater. XXXX, XXX, XXX–XXX

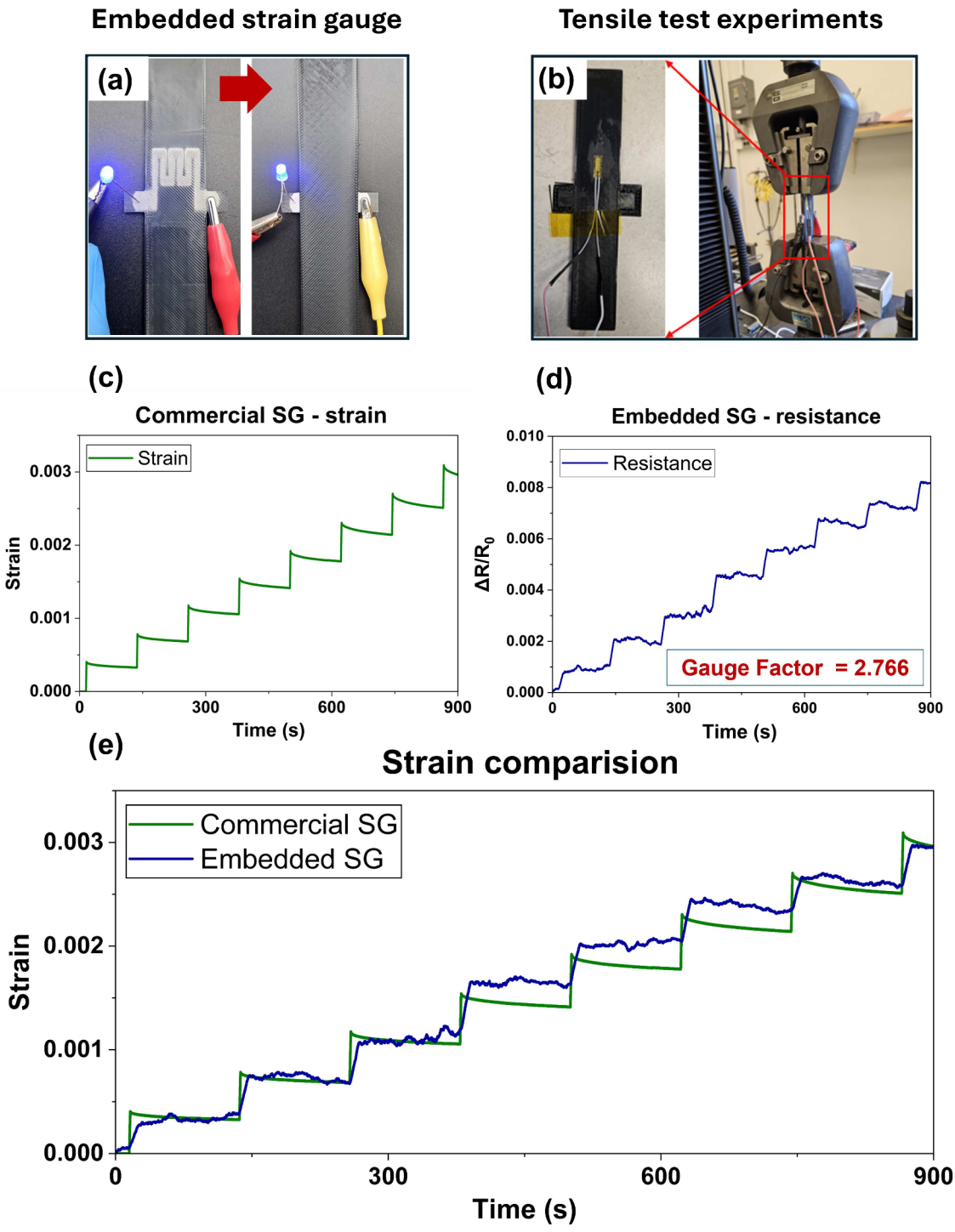


Figure 6. Performance evaluation of the embedded SG: (a) fully additively manufactured embedded SG; (b) experimental setup for quasi-static tensile testing; (c) strain response of the commercial SG during quasi-static tensile loading; (d) resistance response of the embedded SG and gauge factor determination using the commercial SG as the reference; and (e) comparison of the strain measured by the embedded and commercial SGs.

applied strain throughout the loading cycle, demonstrating that the proposed AM approach provides electromechanical sensing while eliminating the need for adhesive bonding, secondary sensor integration, or post-processing.

$$\text{Gauge Factor (GF)} = \frac{\frac{\Delta R}{R}}{\frac{\Delta L}{L}} = \frac{\Delta R}{R_0 \cdot \varepsilon} \quad (2)$$

4.4.2. Embedded Energy Harvesting. To demonstrate the energy-harvesting capability of the proposed hybrid AM approach, a flexible triboelectric nanogenerator (TENG)[33] was fabricated and evaluated. In this application, TPU was selected as the host material owing to its excellent flexibility, elasticity, and mechanical durability,[45] which enable repeated deformation under cyclic loading while maintaining stable triboelectric performance. Its compliant nature also facilitates conformal contact and

Downloaded from pubs.acs.org/aaembp/article-pdf/doi/10.1021/acsaelm.6c01769/6916596/el-2026-017696.pdf by RENSSELAER POLYTECHNIC INST user on 12 November 2026

https://doi.org/10.1021/acsaelm.6c01769
ACS Appl. Electron. Mater. XXXX, XXX, XXX−XXX

separation between the triboelectric layers, making TPU well suited for flexible energy harvesting applications.

As shown in Figure 7a, the device consists of a multilayer sandwich architecture with CSAM electrodes embedded between sequentially overprinted TPU layers. The fabrication process involved alternating FFF printing and CSAM metallization to sequentially form the lower electrode, encapsulation layer, upper electrode, and final protective TPU layer (Figure 7b). This fully additive manufacturing strategy eliminates secondary bonding and separate spacer layers while improving structural integrity, mechanical flexibility, and manufacturing simplicity, resulting in a flexible energy-harvesting device.

The electrical output performance of the flexible TENG was evaluated under pneumatic actuation using the experimental

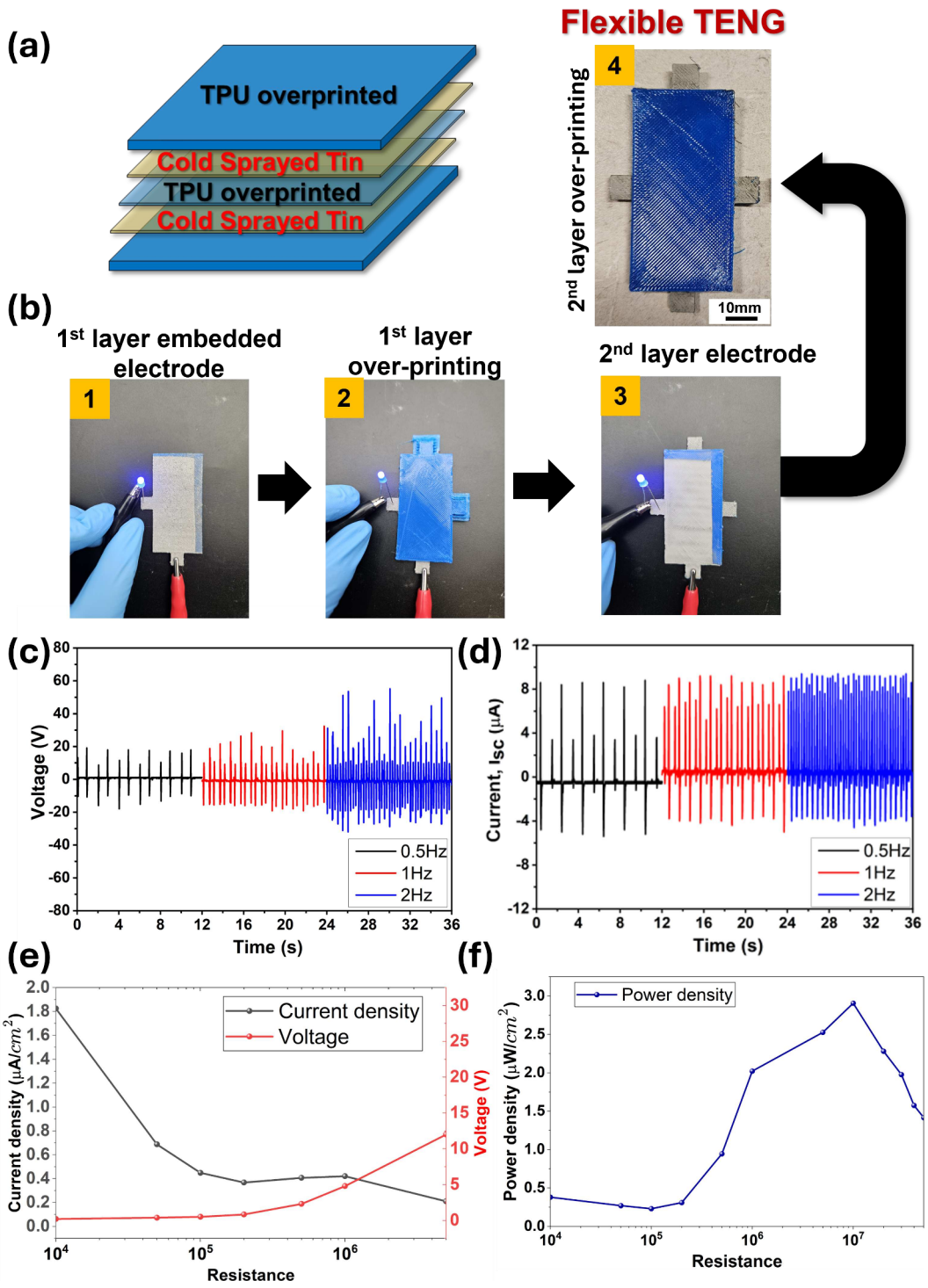


Figure 7. Fully additively manufactured TENG and its performance evaluation: (a) schematic of the embedded TENG architecture; (b) fabrication process; (c) open-circuit voltage (V_{oc}) as a function of excitation frequency; (d) short-circuit current (I_{sc}) as a function of excitation frequency; (e) output voltage and current density as a function of external load resistance; and (f) output power density as a function of external load resistance.

https://doi.org/10.1021/acsaelm.6c01769
ACS Appl. Electron. Mater. XXXX, XXX, XXX−XXX

Downloaded from pubs.acs.org/aaembp/article-pdf/doi/10.1021/acsaelm.6c01769/6916967/el-2026-017696.pdf by RENSSELAER POLYTECHNIC INST user on 12 November 2026

setup shown in Figure S7 (Supporting Information). The device was tested under applied pressures ranging from 25 to 40 psi and excitation frequencies between 0.5 and 2 Hz (Figure S8, Supporting Information). As shown in Figure 7c,d, both the open-circuit voltage (V_{oc}) and short-circuit current (I_{sc}) increased steadily with increasing applied pressure and excitation frequency, reaching maximum values of 65 V and 9 μA, respectively, at 40 psi and 2 Hz. The enhanced electrical output is attributed to the higher contact pressure and increased contact−separation frequency, which increase the effective contact area and triboelectric charge density at the TPU interface, resulting in stronger electrostatic induction during the separation process and more efficient charge transfer.

To evaluate the practical power output of the device, the TENG was coupled with a full-bridge rectifier and tested across external load resistances ranging from 10 kΩ to 40 MΩ (Figure 7e,f). As the external load resistance increased, the output voltage increased while the current density decreased, resulting in the characteristic impedance-dependent behavior of TENG devices. Consequently, the output power ($P = V^2/R$) initially increased, reaching a peak power density of 3 μW/cm^2 at 10 MΩ, before decreasing at higher load resistances, indicating effective impedance matching between the TENG and the external load. Overall, these results demonstrate that the proposed hybrid AM strategy enables the fabrication of mechanically flexible and electrically efficient TENGs. By embedding both electrodes directly within the polymer structure, the proposed approach eliminates secondary bonding while improving mechanical robustness and structural integrity. The fully AM workflow also provides the design flexibility needed to fabricate conformal energy harvesters for wearable electronics, soft robotics, and intelligent polymer structures.

4.4.3. Embedded Wireless Communication. To demonstrate the wireless communication capability of the proposed AM approach, an RFID tag was selected as a representative application. As shown in Figure 8a, CSAM metallization served as the conductive interconnect between the RFID antenna and integrated circuit (IC) (*MIFARE, M1*), enabling direct electrical integration on the 3D-printed PLA substrate. Following antenna−IC integration, the RFID tag was embedded within the polymer host structure, fully encapsulating the antenna and conductive interconnects within the printed component (Figure 8a). Notably, this demonstration highlights the capability of the proposed approach to directly print conductive interconnects, eliminating the need for conventional wiring, adhesive bonding, and secondary assembly steps.

The functionality of the embedded RFID tag was evaluated using a 13.56 MHz RFID reader (*Adafruit, PN532*) connected to an Arduino Uno. As shown in Figure 8b, the embedded RFID tag was successfully detected, and the unique identifier (UID) of the RFID IC was correctly displayed on the Arduino serial monitor, confirming successful wireless communication (see Video S2, Supporting Information). The successful operation of the RFID tag after overprinting demonstrates that the cold-sprayed conductive interconnect maintained both electrical continuity and sufficient signal integrity despite complete encapsulation within the polymer structure. Unlike conventionally attached RFID tags, the proposed manufacturing strategy fully encapsulates the conductive interconnects within the polymer component, providing enhanced protection against mechanical damage and environmental exposure. This capability is particularly attractive for smart manufacturing and structural health monitoring applications, where embedded identification enables product traceability, lifecycle monitoring, and digital-twin integration.

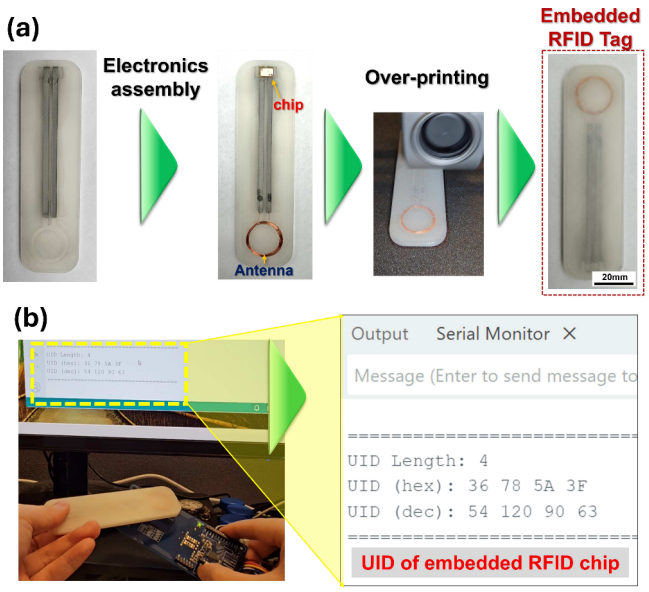


Figure 8. Embedded RFID application: (a) fabrication process of the fully embedded RFID tag and (b) functional validation of the embedded RFID tag using a 13.56 MHz RFID reader.

Collectively, these demonstrations highlight the versatility of the proposed hybrid AM strategy for fabricating multifunctional polymer structures with embedded sensing, wireless communication, and energy-harvesting capabilities. By integrating these complementary functionalities within a single manufacturing workflow, the proposed approach enables the fabrication of smart polymer systems without secondary assembly, adhesive bonding, chemical metallization, or post-processing. This scalable manufacturing platform provides a promising pathway toward next-generation smart structures for structural health monitoring, wearable electronics, soft robotics, and cyber-physical systems.

5. CONCLUSION

This work developed a multimaterial hybrid AM strategy that combines material extrusion and solid-state cold spray metallization to directly fabricate and encapsulate metallic electronic features within polymer structures without chemical processing, thermal sintering, or secondary bonding. The study established the processing−structure−property relationships governing cold spray polymer metallization and demonstrated the feasibility of manufacturing multifunctional smart polymer structures. The main conclusions are as follows:

- Process optimization identified gas temperature, gas pressure, and nozzle traverse speed as the key parameters governing electrical resistance and deposition width. An optimal processing condition of 200 °C, 0.6 MPa, and 150 mm/s balanced electrical performance and polymer protection.
- Microstructural characterization showed that the optimized condition produced a continuous, well-consolidated coating with a thickness of 45−62 μm and a promising adhesion strength of ∼7 MPa.

https://doi.org/10.1021/acsaelm.6c01769
ACS Appl. Electron. Mater. XXXX, XXX, XXX−XXX

Downloaded from pubs.acs.org/aaembp/article-pdf/doi/10.1021/acsaelm.6c01769/6916596/7/el-2026-017696.pdf by RENSSELAER POLYTECHNIC INST user on 12 November 2026

- The proposed approach achieved fully embedded, electrically functional electrodes with an electrical conductivity of 3.76×10^5 S m^{-1}, which is within one order of magnitude of bulk Sn.
- The approach successfully enabled embedded strain sensing, triboelectric energy harvesting, and wireless communication. The embedded SG achieved a GF of 2.766, the flexible TENG generated up to 65 V, 9 μA, and a peak power density of 3 μW/cm^2, and the RFID tag remained functional after overprinting.

Overall, the proposed hybrid AM strategy provides a scalable platform for multimaterial additive manufacturing by integrating structural polymers and functional metallic features within monolithic 3D-printed components. This approach may enable smart structures for structural health monitoring, soft robotics, wearable electronics, and cyber-physical systems. Future work will extend the proposed platform to a wider range of structural, conductive, and functional materials toward multimaterial AM of intelligent engineering systems.

■ ASSOCIATED CONTENT

Supporting Information

The Supporting Information is available free of charge at https://pubs.acs.org/doi/10.1021/acsaelm.6c01769.

Feedstock powder characterization (Figure S1); strain gauge (SG) design (Figure S2); pattern fidelity evaluation method (Figure S3); cross-cut and pull-off adhesion test method (Figure S4); pull-off adhesion test of overprinted layer (Figure S5); mechanical characterization of the 3D-printed host structure (Figure S6); custom-designed pneumatic impact testing system for TENG characterization (Figure S7); electrical output of the embedded TENG under various impact loading conditions (Figure S8); and ANOVA results of cold spray metallization (Table S1) (PDF)

Video S1: Overprinting of a cold spray direct-written strain gauge by fused filament fabrication (MP4)

Video S2: Experimental validation of the embedded RFID tag (MP4)

Video S3: Thermomechanical response of the host polymer structure, accompanied by thermal camera measurements (MP4)

■ AUTHOR INFORMATION

Corresponding Author

Semih Akin − *Department of Mechanical, Aerospace and Nuclear Engineering, Rensselaer Polytechnic Institute, Troy, New York 12180, United States; Center for Smart Convergent Manufacturing Systems (CSCMS), Rensselaer Polytechnic Institute, Troy, New York 12180, United States;* orcid.org/0000-0002-3644-7133; Email: akins@rpi.edu

Authors

Jaehun Jeon − *Department of Mechanical, Aerospace and Nuclear Engineering, Rensselaer Polytechnic Institute, Troy, New York 12180, United States*

SK Shamim Hasan Abir − *Department of Mechanical, Aerospace and Nuclear Engineering, Rensselaer Polytechnic Institute, Troy, New York 12180, United States;* orcid.org/0000-0003-4079-1006

Shinan Huang − *Department of Mechanical, Aerospace and Nuclear Engineering, Rensselaer Polytechnic Institute, Troy, New York 12180, United States*

Joni Dhar − *Department of Mechanical, Aerospace and Nuclear Engineering, Rensselaer Polytechnic Institute, Troy, New York 12180, United States*

Grace Richard − *Department of Mechanical, Aerospace and Nuclear Engineering, Rensselaer Polytechnic Institute, Troy, New York 12180, United States*

Akshay R. Ananda − *Department of Mechanical, Aerospace and Nuclear Engineering, Rensselaer Polytechnic Institute, Troy, New York 12180, United States*

Fotis Kopsaftopoulos − *Department of Mechanical, Aerospace and Nuclear Engineering, Rensselaer Polytechnic Institute, Troy, New York 12180, United States; Center for Smart Convergent Manufacturing Systems (CSCMS), Rensselaer Polytechnic Institute, Troy, New York 12180, United States*

Johnson Samuel − *Department of Mechanical, Aerospace and Nuclear Engineering, Rensselaer Polytechnic Institute, Troy, New York 12180, United States; Center for Smart Convergent Manufacturing Systems (CSCMS), Rensselaer Polytechnic Institute, Troy, New York 12180, United States*

Complete contact information is available at: https://pubs.acs.org/doi/10.1021/acsaelm.6c01769

Author Contributions

J.J. and S.A. conceived the project. The manuscript was written through contributions of all authors. All authors have given approval to the final version of the manuscript.

Notes

During manuscript preparation, ChatGPT (OpenAI, GPT-6) was used solely for language refinement and grammatical corrections. The tool was not used to generate scientific content. All results, interpretations, and conclusions are the authors' original work and have been carefully reviewed and validated. The authors declare no competing financial interest.

■ ACKNOWLEDGMENTS

The authors acknowledge the internal funding support from the Department of Mechanical, Aerospace, and Nuclear Engineering (MANE) at Rensselaer Polytechnic Institute (RPI). The authors also gratefully acknowledge NYSTAR's support (Contract No. C250128) through RPI's New York State-designated Center for Advanced Technology, the Center for Smart Convergent Manufacturing Systems (CSCMS).

■ REFERENCES

(1) Park, S.; Shou, W.; Makatura, L.; Matusik, W.; Fu, K. K. 3D printing of polymer composites: Materials, processes, and applications. *Matter* **2022**, *5*, 43−76.

(2) Chowdhury, A. H.; John, D.; Lama, A.; Murickan, R. T.; Agarwal, A. Cold-Spray Enabled Scalable Manufacturing of Flexible Graphene-Based Wearable Sensors. *ACS Appl. Electron. Mater.* **2026**, *8*, 7692−7704.

(3) MacDonald, E.; Wicker, R. Multiprocess 3D printing for increasing component functionality. *Science* **2016**, *353*, eaaf2093.

Downloaded from pubs.acs.org/aaemp/article-pdf/doi/10.1021/acsaelm.6c01769/6916596 7/el-2026-017696.pdf by RENSSELAER POLYTECHNIC INST user on 12 November 2026

(4) Tan, H. W.; Choong, Y. Y. C.; Kuo, C. N.; Low, H. Y.; Chua, C. K. 3D printed electronics: Processes, materials and future trends. *Prog. Mater. Sci.* **2022**, *127*, 100945.
(5) Akbari, S.; Kostov, K.; Lim, J.-K.; Murthy, H. K.; Bakowski, M.; Wang, Q.; Salter, M.; Andersson, D.; Brinkfeldt, K. Fully printed ultra-thin embedded electronics package for wide band gap power semiconductor devices using multimaterial inkjet additive manufacturing. *Prog. Addit. Manuf.* **2025**, *10*, 7241−7249.
(6) Yu, K.; Zhang, W.; Feng, J.; Yue, J.; Ding, Y.; Liang, Q.; Cao, Y.; Li, D.; He, J. Multi-material printing of 3D heterogeneous structures with embedded microscale conductive features for electromagnetic function. *Addit. Manuf.* **2025**, *109*, 104890.
(7) Muth, J. T.; Vogt, D. M.; Truby, R. L.; Mengüç, Y.; Kolesky, D. B.; Wood, R. J.; Lewis, J. A. Embedded 3D printing of strain sensors within highly stretchable elastomers. *Adv. Mater.* **2014**, *26*, 6307−6312.
(8) Khosravani, M. R.; Reinicke, T. 3D-printed sensors: Current progress and future challenges. *Sens. Actuators, A* **2020**, *305*, 111916.
(9) De, S.; Xu, S.; Tang, Y.; Jackson, A.; Wang, P. L.; Rukmani, S. J.; McDonald, E.; Zhao, X.; Duty, C.; Roschli, A.; et al. Printing the future of strain measurement: Flexible sensors via additive manufacturing for wearables, robotics, and smart infrastructure. *Sens. Int.* **2026**, *7*, 100375.
(10) Ahmed, S.; Bodaghi, M.; Nauman, S.; Muhammad Khan, Z. Additive manufacturing of flexible strain sensors based on smart composites for structural health monitoring with high accuracy and fidelity. *Adv. Eng. Mater.* **2023**, *25*, 2300763.
(11) Lazarus, N.; Tyler, J. B.; Cardenas, J. A.; Hanrahan, B.; Tsang, H.; Bedair, S. S. Direct electroless plating of conductive thermoplastics for selective metallization of 3D printed parts. *Addit. Manuf.* **2022**, *55*, 102793.
(12) Juarez, T.; Schroer, A.; Schwaiger, R.; Hodge, A. M. Evaluating sputter deposited metal coatings on 3D printed polymer micro-truss structures. *Mater. Des.* **2018**, *140*, 442−450.
(13) Aktitiz, I.; Daricik, F.; Aydin, A.; Aydn, K. Metallization of 3D printed polylactic acid polymer structures via radio-frequency sputtering. *J. Mater. Eng. Performance* **2025**, *34*, 8610−8624.
(14) Valentine, A. D.; Busbee, T. A.; Boley, J. W.; Raney, J. R.; Chortos, A.; Kotikian, A.; Berrigan, J. D.; Durstock, M. F.; Lewis, J. A. Hybrid 3D printing of soft electronics. *Adv. Mater.* **2017**, *29*, 1703817.
(15) Rahman, M. T.; Bone, J.; Roussel, T. J.; Jenkins, J. L.; Huckaba, A. J. Hybrid Fabrication of an Electrochemical Electrode via Inkjet Printing on 3D-Printed Substrates. *ACS Omega* **2026**, *11*, 24053..
(16) Gooding, J.; Fields, T. 3d printed strain gauge geometry and orientation for embedded sensing. *58th AIAA/ASCE/AHS/ASC Structures, Structural Dynamics, and Materials Conference*, **2017**; p 0350.
(17) Sahoo, S.; Panja, S. C.; Kumar, V.; Sarkar, D. A Sustainable Approach to Plastronics: Dip-Coating-Assisted Area-Selective Metallization of 3D-Printed Polymer Substrates. *ACS Appl. Polym. Mater.* **2026**, *8*, 2746−2761.
(18) Tan, K. Y.; Poh, W. S.; Endot, N. A.; Khiew, P. S.; Foo, C. Y.; Lim, H. N. Freeze-dried silver nanowire based resin formulation for vat photopolymerization 3D printing of stretchable and electrically conductive nanocomposites. *Addit. Manuf.* **2025**, *101*, 104706.
(19) Rahman, S.; Akin, S.; Ren, J.; Zhou, P.; Kopsaftopoulos, F.; Samuel, J. Additively manufactured smart metallic structures with embedded sensing: a review. *Prog. Addit. Manuf.* **2026**, *11*, 2521−2562.
(20) Melentiev, R.; Yu, N.; Lubineau, G. Polymer metallization via cold spray additive manufacturing: A review of process control, coating qualities, and prospective applications. *Addit. Manuf.* **2021**, *48*, 102459.
(21) Rezzoug, A.; Gholenji, R.; Yandouzi, M. Innovative Thermal Spray Deposition Techniques for Polymer and Polymeric Matrix Composite Substrates: Methodologies, Characteristics, and Real-World Applications. *J. Therm. Spray Technol.* **2025**, *34*, 2037−2080.
(22) Tsai, J.-T.; Akin, S.; Zhou, F.; Bahr, D. F.; Jun, M. B.-G. Establishing a cold spray particle deposition window on polymer substrate. *Journal of Thermal Spray Technology* **2021**, *30*, 1069−1080.
(23) Akin, S.; Lee, S.; Jo, S.; Ruzgar, D. G.; Subramaniam, K.; Tsai, J.-T.; Jun, M. B.-G. Cold spray-based rapid and scalable production of printed flexible electronics. *Addit. Manuf.* **2022**, *60*, 103244.
(24) Akin, S.; Kim, Y. W.; Xu, S.; Nath, C.; Wu, W.; Jun, M. B.-G. Cold spray direct writing of flexible electrodes for enhanced performance triboelectric nanogenerators. *J. Manuf. Process.* **2023**, *100*, 27−33.
(25) Sahoo, S.; Panja, S. C.; Sarkar, D.; Saha, R. Direct surface-exposed nucleation site development via a dip-coated filament strategy for facile functional metallization in material extrusion-based plastronics. *ACS Appl. Electron. Mater.* **2026**, *8*, 92−110.
(26) Huang, H.-J.; Zhou, M.-B.; Zhang, X.-P. Ingenious Method for Rapid Fabrication of a Highly Conductive Hybrid Film of Printed Cu Nanoparticle Layers Plated by Ag Nanoplates on a PET Substrate at Room Temperature. *ACS Appl. Electron. Mater.* **2021**, *3*, 4640−4648.
(27) Hu, K.; Zhou, Y.; Sitaraman, S. K.; Tentzeris, M. M. Additively manufactured flexible on-package phased array antennas for 5G/mmWave wearable and conformal digital twin and massive MIMO applications. *Sci. Rep.* **2023**, *13*, 12515.
(28) Crapnell, R. D.; Bernalte, E.; Banks, C. E. Advances in additive manufacturing electrochemistry. *Chem. Rev.* **2026**, *126*, 6963.
(29) Akin, S.; Nath, C.; Jun, M. B.-G. Selective surface metallization of 3D-printed polymers by cold-spray-assisted electroless deposition. *ACS Appl. Electron. Mater.* **2023**, *5*, 5164−5175.
(30) Cojocaru, V.; Frunzaverde, D.; Miclosina, C.-O.; Marginean, G. The influence of the process parameters on the mechanical properties of PLA specimens produced by fused filament fabrication—A review. *Polymers* **2022**, *14*, 886.
(31) Johar, M.; Rosli, A. A.; Shuib, R. K.; Abdul Hamid, Z. A.; Abdullah, M. K.; Ku Ishak, K. M.; Rusli, A. Dimensional stability of poly (lactic acid)(PLA) parts fabricated using fused deposition modelling (FDM). *Prog. Rubber Plast. Recycl. Technol.* **2025**, *41*, 218−232.
(32) Marco, V.; Massimo, G.; Manuela, G. Additive manufacturing of flexible thermoplastic polyurethane (TPU): enhancing the material elongation through process optimisation. *Prog. Addit. Manuf.* **2025**, *10*, 2877−2891.
(33) Akin, S.; Chang, T.; Abir, S. S. H.; Kim, Y. W.; Xu, S.; Lim, J.; Sim, Y.; Lee, J.; Tsai, J.-T.; Nath, C.; et al. One-step fabrication of functionalized electrodes on 3D-printed polymers for triboelectric nanogenerators. *Nano Energy* **2024**, *129*, 110082.
(34) Wang, Z.; Mao, P.; Huang, C.; Yu, P.; Li, W.; Yin, S. Deposition mechanism of ceramic reinforced metal matrix composites via cold spraying. *Addit. Manuf.* **2024**, *85*, 104167.
(35) Guo, D.; Kazasidis, M.; Hawkins, A.; Fan, N.; Leclerc, Z.; MacDonald, D.; Nastic, A.; Nikbakht, R.; Ortiz-Fernandez, R.; Rahmati, S.; et al. Cold spray: over 30 years of development toward a hot future. *J. Therm. Spray Technol.* **2022**, *31*, 866−907.
(36) Champagne, V.; Helfritch, D. The unique abilities of cold spray deposition. *Int. Mater. Rev.* **2016**, *61*, 437−455.
(37) Li, J.; Yang, J.; Wang, P.; Chen, X.; Jiang, M.; Zhang, H.; Wang, G.; Liu, F.; Xiang, Z.; Chen, M. Laser-activated metallization-based hybrid additive manufacturing technology for 3D flexible electronics. *ACS Appl. Polym. Mater.* **2025**, *7*, 1969−1978.
(38) Bernasconi, R.; Rogiers, P.; Magagnin, L. Self-Activating Resins for the Straightforward Electroless Metallization of 3D Printed Parts. *Addit. Manuf.* **2026**, *119*, 105129.
(39) Gerges, T.; Semet, V.; Lombard, P.; Allard, B.; Cabrera, M. Rapid 3D-Plastronics prototyping by selective metallization of 3D printed parts. *Addit. Manuf.* **2023**, *73*, 103673.
(40) Wu, C.-H.; Palao, J. E. Cold spray surface patterning of aluminum on aluminum, silicon, glass, and printed circuit board substrates. *Surf. Coat. Technol.* **2018**, *349*, 928−940.
(41) Parodo, G.; Moffa, G.; Silvestri, A.; Sorrentino, L.; Testa, G.; Turchetta, S. Influence of surface treatments on the pull-off performance of adhesively bonded polylactic acid (PLA) specimens manufactured by fused deposition modeling (FDM). *Materials* **2025**, *18*, 3965.
(42) Campos-Jurado, M.; Rodríguez-Alabanda, Ó.; Guerrero-Vacas, G. Manufacturing of polymer−metal composite by fused filament fabrication: adhesion of PLA and PETG on aluminum. *Polymers* **2025**, *17*, 2210.

Downloaded from pubs.acs.org/aaemp/article-pdf/doi/10.1021/acsaelm.6c01769/6916967/el-2026-017696.pdf by RENSSELAER POLYTECHNIC INST user on 12 November 2026

(43) Billings, C.; Siddique, R.; Liu, Y. Photocurable polymer-based 3D printing: Advanced flexible strain sensors for human kinematics monitoring. *Polymers* **2023**, *15*, 4170.
(44) Huang, Y.-T.; Huang, S.-C.; Hsu, C.-C.; Chao, R.-M.; Vu, T. K. Design and fabrication of single-walled carbon nanonet flexible strain sensors. *Sensors* **2012**, *12*, 3269−3280.
(45) Zhang, W.; Liu, Q.; Chao, S.; Liu, R.; Cui, X.; Sun, Y.; Ouyang, H.; Li, Z. Ultrathin stretchable triboelectric nanogenerators improved by postcharging electrode material. *ACS Appl. Mater. Interfaces* **2021**, *13*, 42966−42976.

Downloaded from pubs.acs.org/aaembp/article-pdf/doi/10.1021/acsaelm.6c01769/6916596 7/el-2026-017696.pdf by RENSSELAER POLYTECHNIC INST user on 12 November 2026

https://doi.org/10.1021/acsaelm.6c01769
ACS Appl. Electron. Mater. XXXX, XXX, XXX−XXX